Manifold Regularizer for High-Resolution fMRI Joint Reconstruction and Dynamic Quantification

Shouchang Guo, Jeffrey A. Fessler, *Fellow, IEEE*, and Douglas C. Noll, *Fellow, IEEE*

***Abstract*— Oscillating Steady-State Imaging (OSSI) is a recently developed fMRI acquisition method that can provide 2 to 3 times higher SNR than standard fMRI approaches. However, because the OSSI signal exhibits a nonlinear oscillation pattern, one must acquire and combine n_c (e.g., 10) OSSI images to get an image that is free of oscillation for fMRI, and fully sampled acquisitions would compromise temporal resolution. To improve temporal resolution and accurately model the nonlinearity of OSSI signals, instead of using subspace models that are not well suited for the data, we build the MR physics for OSSI signal generation as a regularizer for the undersampled reconstruction. Our proposed physics-based manifold model turns the disadvantages of OSSI acquisition into advantages and enables joint reconstruction and quantification. OSSI manifold model (OSSIMM) outperforms subspace models and reconstructs high-resolution fMRI images with a factor of 12 acceleration and without spatial or temporal smoothing. Furthermore, OSSIMM can dynamically quantify important physics parameters, including R_2^* maps, with a temporal resolution of 150 ms.**

***Index Terms*— Manifold model, high-resolution fMRI, quantitative MRI, R_2^*, oscillating steady-state imaging (OSSI), joint reconstruction and quantification.**

I. Introduction

FUNCTIONAL magnetic resonance imaging (fMRI) is an important tool for brain research and diagnosis. In its most common form, it detects functional activation by acquiring a time-series of MR images with blood-oxygen-level-dependent (BOLD) contrast [1]. However, the BOLD effect has a relatively low signal-to-noise ratio (SNR) [2], and the SNR further decreases with improved spatial resolution. Because the functional units (cortical columns) of the brain are on the order of 1 mm, high resolution with high SNR is critical for some fMRI experiments. This paper focuses on Oscillating Steady-State Imaging (OSSI), a recent fMRI acquisition approach that provides higher SNR signals than standard gradient-echo (GRE) imaging [3].

Oscillating Steady-State Imaging (OSSI) establishes a new steady state by combining balanced gradients as in balanced steady-state free precession [4] and quadratic RF phase progression as in RF-spoiled GRE [5]. This steady-state signal combines the high SNR feature of the balanced steady state and the T_2^* contrast of GRE imaging, and presents 2 to 3 times higher SNR than standard GRE fMRI [3], [6]. However, the SNR advantage of OSSI comes at a price of spatial and temporal resolutions. OSSI applies a quadratic RF phase cycling $\phi(n) = \pi n^2/n_c$, where n is the RF index and a typical cycle length is $n_c = 10$. The corresponding OSSI signal oscillates with a periodicity of $n_c \cdot \mathrm{TR}$, and OSSI images exhibit a periodic oscillation pattern as shown in Fig. 1. Therefore, every OSSI image is acquired with a different RF phase across the period, and one must acquire n_c images and combine them to eliminate oscillations for each fMRI image in a regular fMRI time course. Acquiring n_c times more images compromises temporal resolution, and the short TR necessary for OSSI acquisition can limit single-shot spatial resolution.

To improve the spatial-temporal resolution, we previously used a patch-tensor low-rank model for the sparsely undersampled reconstruction [6]. While low-rank regularization fits data to linear subspaces, previous works [6], [7] show that OSSI images across the period of $n_c \cdot \mathrm{TR}$ are not very low-rank, because the oscillation patterns in OSSI images are nonlinear and cannot be accurately modeled by linear subspace models. Instead of imposing subspace models [8] such as low-rankness and/or sparsity that may or may not suit the data, this paper proposes a nonlinear dimension reduction approach for OSSI reconstruction that uses a MR physics-based manifold as a regularizer, inspired by parameter map reconstruction methods for MR fingerprinting [9], [10].

Manifold learning is a well-established area of research in machine learning [11]. In MRI, several studies have explored different manifold modeling and learning approaches. For example, [12] proposes an unrolled network for accelerated cardiac MRI imaging that utilizes a low-rank tensor manifold. [13] exploits image patch similarity with a low-dimensional patch manifold for sparsely sampled MR image reconstruction. Furthermore, [14] reconstructs MR fingerprinting images with

Manuscript received 9 December 2023; revised 3 March 2024; accepted 20 March 2024. Date of publication 25 March 2024; date of current version 1 August 2024. This work was supported in part by the National Institute of Biomedical Imaging and Bioengineering (NIBIB) and in part by the National Institute of Neurological Disorders and Stroke (NINDS) through Grant R01 EB023618 and Grant U01 EB026977. *(Corresponding author: Shouchang Guo.)*

This work involved human subjects in its research. Approval of all ethical and experimental procedures and protocols was granted by the University of Michigan Medical School Institutional Review Board.

Shouchang Guo was with the Department of Electrical Engineering and Computer Science, University of Michigan, Ann Arbor, MI 48109 USA. She is now with the Functional MRI Lab, University of Michigan, Ann Arbor, MI 48109 USA (e-mail: shoucguo@umich.edu).

Jeffrey A. Fessler is with the Department of Electrical Engineering and Computer Science, University of Michigan, Ann Arbor, MI 48109 USA (e-mail: fessler@umich.edu).

Douglas C. Noll is with the Department of Biomedical Engineering, University of Michigan, Ann Arbor, MI 48109 USA (e-mail: dnoll@umich.edu).

Digital Object Identifier 10.1109/TMI.2024.3381197

temporal low-rank and spatial regularizations, in addition to the Bloch manifold regularization. Regarding fMRI, with the assumption that time-varying functional connectivity data lie on a low-dimensional manifold, [15] and [16] exploit manifold learning techniques for task-based functional connectivity analysis. Reference [17] provides multi-modal brain representations by embedding local image features to a low-dimensional manifold. Our work appears to be the first to achieve joint undersampled reconstruction and quantization in fMRI, enabled by the proposed manifold regularization of OSSI signals.

As outlined in Fig. 1, the proposed manifold model focuses on MR physics for OSSI signal generation. It represents n_c OSSI signal values per voxel by just 3 physical parameters, via Bloch equations. The nonlinear nature of the Bloch equations enables nonlinear representations of the data and nonlinear dimension reduction. We further introduce a near-manifold regularizer that encourages the reconstructed signal values to lie near the manifold. Compared to quantitative imaging methods that strive to constrain the reconstructed images to exactly match the physics-based representations [9], [10], [18], [19], the proposed regularizer encourages the images to be near the manifold while also allowing for potential model mismatch.

In fMRI, $R_2' = 1/T_2'$ relates to susceptibility properties of blood and captures BOLD changes [20]. The R_2 relaxation with $R_2 = 1/T_2$ describes the irreversible MR signal decay and is tissue dependent. f_0 denotes off-resonance frequency due to B_0 field inhomogeneity. The BOLD response that arises from neural activity can be expressed as the convolution of hemodynamic response function (HRF) and the stimulus function (or task waveform) [21].

Changes in R_2' or R_2^*, where $R_2^* = R_2 + R_2'$, depend on neural activity, so one can use dynamic quantification of R_2' or R_2^* to monitor brain activity. Furthermore, because R_2^* is sensitive to iron concentration, quantifying R_2^* is important in clinical protocols for state changes of diseases such as Alzheimer's or Parkinson's disease [22]. However, standard T_2^*-weighted magnitude images only assess relative signal changes due to BOLD effects and are not quantitative in terms of BOLD-dependent parameters like T_2^* or T_2' [23], [24], [25]. By constructing a T_2' driven physics manifold based on BOLD-induced intravoxel dephasing, our work demonstrates the utility of the OSSI manifold model for dynamic quantification of T_2^* or R_2^*.

This paper shows that the proposed physics-based manifold and near-manifold regularizer can jointly optimize OSSI images and quantitative maps. The manifold model enables high-resolution OSSI fMRI with 12-fold acquisition acceleration, outperforms low-rank regularization with more functional activation, and provides quantitative and dynamic assessment of tissue R_2^* maps and off-resonance f_0, with a temporal resolution of 150 ms.

II. OSSI Manifold Model (OSSIMM)

OSSI signals oscillate with a periodicity of n_cTR, and the OSSI fMRI time course contains n_c images for every image in a regular fMRI time series. We refer to the fast acquisition dimension of size n_c as "fast time" and the regular fMRI time dimension as "slow time" as presented in Fig. 1. OSSI fast time signals can have different shapes and change nonlinearly with respect to MR physics parameters, as illustrated in Figs. 1 and 2. To accurately model the nonlinear oscillations, we propose a MR-physics based manifold model for the undersampled reconstruction.

A. Physics-Based Manifold

In OSSI, the steady-state transverse magnetization of one isocromat at observation time t for all n_c fast time points is

$$m_0\,\boldsymbol{\phi}(t;\,T_1,\,T_2,\,f_0),$$

where $m_0 \in \mathbb{C}$ is the equilibrium magnetization, $\boldsymbol{\phi}(\cdot) \in \mathbb{C}^{n_c}$ represents MR physics that is described and calculated by steady-state Bloch equations, T_1 and T_2 are tissue relaxation times, and f_0 denotes central off-resonance frequency from B_0 field inhomogeneity.

We model the T_2'-weighted OSSI signal in a voxel with an intra-voxel spreading of off-resonance frequencies f as:

$$\begin{aligned} &m_0\boldsymbol{\Phi}(t;\,T_2',\,f_0;\,T_1,\,T_2) \\ &\triangleq \int_{-\infty}^{\infty} m_0\boldsymbol{\phi}(t;\,T_1,\,T_2,\,f_0+f)\;p(f;\,T_2')\,\mathrm{d}f\,. \end{aligned}$$

The T_2' exponential decay corresponds to a Cauchy distribution for f with a probability density function (PDF) $p(f) = \gamma/\pi(\gamma^2 + f^2)$, and scale parameter $\gamma = 1/(2\pi T_2')$.

The isocromat signal at time $t > 0$ exhibits T_2 decay and increased off-resonance dephasing due to field inhomogeneity and BOLD-related field changes:

$$\begin{aligned} &m_0\boldsymbol{\phi}(t;\,T_1,\,T_2,\,f_0) \\ &\quad = m_0\boldsymbol{\phi}(t=0;\,T_1,\,T_2,\,f_0)\,\mathrm{e}^{-t/T_2}\,\mathrm{e}^{-\imath 2\pi f_0 t}\,, \end{aligned}$$

where $t = 0$ denotes the time right after the excitation.

As OSSI TR is relatively short (e.g., TR = 15 ms), we neglect the intravoxel dephasing during the readout and approximate the signal at $0 \le t \le$ TR with the signal at the echo time TE. The T_2'-weighted signal becomes

$$\begin{aligned} &m_0\boldsymbol{\Phi}(t;\,T_2',\,f_0;\,T_1,\,T_2) \\ &\approx \int_{-\infty}^{\infty} m_0\boldsymbol{\phi}(\mathrm{TE};\,T_1,\,T_2,\,f_0+f) \\ &\quad \mathrm{e}^{-\mathrm{TE}/T_2}\,\mathrm{e}^{-\imath 2\pi(f_0+f)\mathrm{TE}}\,p(f;\,T_2')\,\mathrm{d}f\,. \end{aligned} \tag{1}$$

T_1 has a signal scaling effect that can be absorbed in m_0 as illustrated in Fig. 2. Furthermore we drop the notation on $t =$ TE hereafter. Accordingly, T_2'-weighted OSSI fast time signals lie on (or near) the physics-based manifold:

$$\{m_0\boldsymbol{\Phi}(T_2',\,f_0;\,T_2) \in \mathbb{C}^{n_c} : m_0 \in \mathbb{C},\; T_2, T_2',\, f_0 \in \mathbb{R}\}, \tag{2}$$

The manifold maps a limited number of physics parameters to the n_c-dimensional oscillating signals via MR physics.

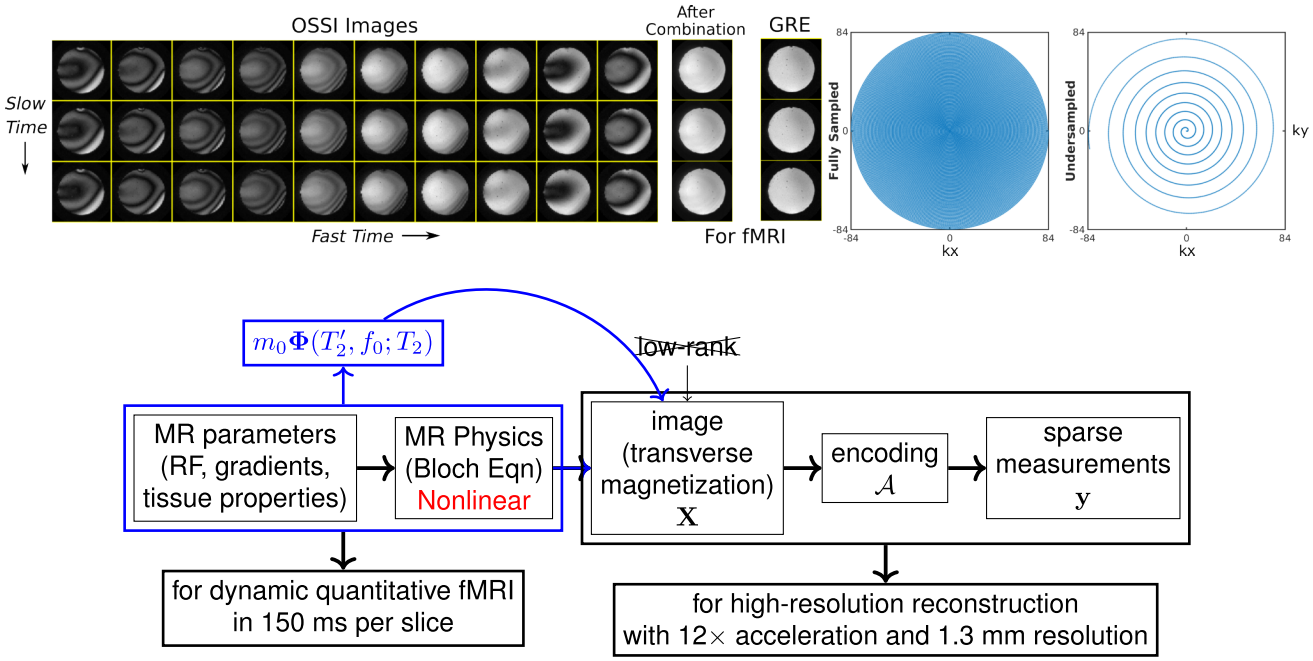

Fig. 1. OSSI oscillation pattern (top left); every set of n_c OSSI "fast time" images are combined for each "slow time" image in an fMRI time series. As illustrated in the diagram (bottom panel), instead of using linear subspace models that might not be a good fit for the data, our proposed manifold model uses the MR physics for the signal generation as a regularizer for the undersampled reconstruction. The undersampled variable-density spiral k-space trajectory is compared to a fully sampled spiral trajectory (top right).

B. Near-Manifold Regularization

The physics-based manifold models the generation of MR signals, enables nonlinear dimension reduction, and can facilitate image reconstruction from undersampled k-space data. Because the physics parameters are location dependent, and because OSSI signal values change drastically with varying parameters as shown in Fig. 2, we model the fast time signals in a voxel-by-voxel manner. Furthermore, to account for potential mismatches due to model simplifications and nonidealities in experiments (e.g., flip angle inhomogeneity), we propose a near-manifold regularizer that encourages the signal values in each voxel to be close to the manifold estimates but not necessarily exactly the same.

The proposed physics manifold model based image reconstruction problem uses the following optimization formulation:

$$\hat{\boldsymbol{X}} = \arg\min_{\boldsymbol{X}} \frac{1}{2}\|\mathcal{A}(\boldsymbol{X}) - \boldsymbol{y}\|_2^2 + \beta \sum_{n=1}^{N} \mathcal{R}\left(\boldsymbol{X}[n,:]\right),$$
$$\mathcal{R}(\boldsymbol{v}) = \min_{m_0, T_2', f_0} \|\boldsymbol{v} - m_0\mathbf{\Phi}(T_2', f_0; T_2)\|_2^2, \tag{3}$$

where $\boldsymbol{X} \in \mathbb{C}^{N\times n_c}$ denotes n_c fast time images to be reconstructed. The vectorized spatial dimension N denotes the number of voxels. $\mathcal{A}(\cdot)$ is a linear operator consisting of coil sensitivities and the non-uniform Fourier transform including undersampling, $\boldsymbol{y}$ represents sparsely sampled k-space measurements. β is the regularization parameter. $\boldsymbol{v} \in \mathbb{C}^{n_c}$ is a vector of fast time signal values for each voxel in $\boldsymbol{X}$, $m_0\mathbf{\Phi}(T_2', f_0; T_2) \in \mathbb{C}^{n_c}$ denotes the manifold estimates. The regularizer minimizes the Euclidean distance between $\boldsymbol{v}$ and $m_0\mathbf{\Phi}(T_2', f_0; T_2)$. T_1 and T_2 are not directly estimated by the model. Section III describes the choices of baseline T_2 values for T_2^* estimation.

Note that with a large enough regularization parameter β, the proposed model would be similar to other quantification works that apply an equality constraint to enforce the images to lie exactly on the manifold. The voxel-wise parametric regularizer $\mathcal{R}(\boldsymbol{v})$ not only performs regularization for the ill-posed reconstruction problem, but also involves parameter estimation and can provide quantitative maps for T_2' and f_0.

C. Optimization Algorithm

To solve (3), we alternate between a regularization update and a data fidelity update for the reconstruction. The minimization of the voxel-wise parametric regularizer w.r.t. m_0, T_2', f_0 for each voxel is a non-convex and nonlinear least-square problem that we solve using the variable projection (VARPRO) method [26], [27]. Let $\boldsymbol{\theta} = [T_2', f_0]$ denote the two nonlinear tissue parameters; the calculation of $\boldsymbol{\theta}$ using VARPRO simplifies to

$$\hat{\boldsymbol{\theta}} = \arg\max_{\boldsymbol{\theta}} \frac{\left|\boldsymbol{v}'\mathbf{\Phi}(\boldsymbol{\theta})\right|^2}{\|\mathbf{\Phi}(\boldsymbol{\theta})\|_2^2}, \tag{4}$$

where $\boldsymbol{v} = \boldsymbol{X}[:, n] \in \mathbb{C}^{n_c}$. Instead of solving (4) for the explicit and sophisticated $\mathbf{\Phi}(\boldsymbol{\theta})$, we construct a dictionary consisting of discrete $\mathbf{\Phi}(\boldsymbol{\theta})$ realizations with varying $\boldsymbol{\theta}$ parameters using Bloch simulations, and then perform grid search to find $\hat{\boldsymbol{\theta}}$ for which $\mathbf{\Phi}(\hat{\boldsymbol{\theta}})$ best matches $\boldsymbol{v}$ according to (4).

Updating m_0 is a least-squares problem with closed-from solution:

$$\hat{m}_0 = \frac{(\mathbf{\Phi}(\hat{\boldsymbol{\theta}}))'\boldsymbol{v}}{\|\mathbf{\Phi}(\hat{\boldsymbol{\theta}})\|_2^2}. \tag{5}$$

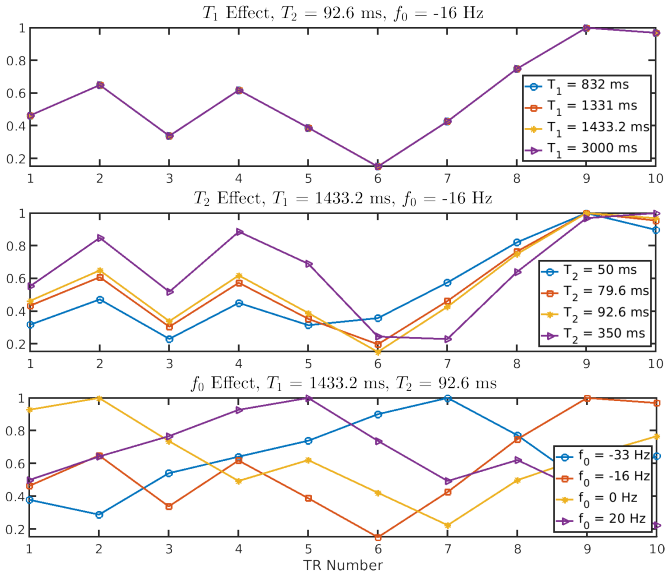

Fig. 2. Normalized OSSI fast time signal magnitude for one isochromat. The change of T_1 only scales OSSI signal values, and the OSSI signal at different T_1s are on top of each other (top panel), while different T_2 and f_0 values lead to different nonlinear oscillations. We further simulated wider ranges of T_2 values and observed that for larger T_2 values (above about 150 ms), the T_2 effect of the OSSI signal is closer to a scaling effect.

We parallelize the regularization update across all voxels.

The update step for $\boldsymbol{X}$ involves a quadratic regularized least-squares problem that we solve using the conjugate gradient method as implemented in the Michigan Image Reconstruction Toolbox [28]. This data fidelity update is easily parallelized across fast time images to speed up the fMRI time series reconstruction.

D. Comparison Method

We compare the manifold approach to a low-rank reconstruction approach that models the fast time signals using linear subspaces. The cost function for this low-rank comparison method is

$$\hat{\boldsymbol{X}} = \arg\min_{\boldsymbol{X}} \tfrac{1}{2}\|\mathcal{A}(\boldsymbol{X}) - \boldsymbol{y}\|_2^2 + \alpha\|\boldsymbol{X}\|_* \tag{6}$$

where $\boldsymbol{X} \in \mathbb{C}^{N\times n_c}$ represents all n_c fast time images, and α is the regularization parameter. Because the composite cost function (6) is convex, nonsmooth, and has a convenient proximal mapping, we solve the optimization problem using the proximal optimized gradient method (POGM) with adaptive restart [29], [30], [31], [32].

III. Simulation Investigations

We generated OSSI signals via Bloch simulation using pulse-sequence parameters that matched the actual data acquisition. We used TR = 15 ms, TE = 2.7 ms (spiral-out trajectory), RF excitation pulse length = 1.6 ms, quadratic RF phase cycling with $\Phi(n) = \pi n^2/n_c$ for nth TR, $n_c = 10$, and flip angle = 10° [3].

A. OSSI Signals

The OSSI signal vector in $\mathbb{C}^{n_c}$ for one isocromat is determined by physics parameters T_1, T_2, and f_0. Fig. 2 presents example OSSI isocromat signals (normalized by the maximum magnitude) with varying physics parameters selected based on gray matter relaxation parameters: $T_1 = 1400$ ms, $T_2 = 92.6$ ms [33]. To approximate (1), we simulated T_2'-weighted OSSI signal in a voxel using a Riemann sum of numerous OSSI isocromat signals at different off-resonance frequencies. Specifically, we calculated a weighted sum of OSSI signals from 4000 isocromats at off-resonance frequency $f_0 + f$, where f uniformly ranged from -200 Hz to 200 Hz, and the weighting function was the PDF of the Cauchy distribution.

We further simulated a fMRI time course for one voxel with time-varying T_2' values. The T_2' waveform is the convolution of the canonical HRF [34] and the fMRI task waveform. Because fMRI percent signal change $\Delta\% \approx \Delta R_2' \cdot \mathrm{TE}_{\mathrm{eff}}$ [35] and OSSI $\mathrm{TE}_{\mathrm{eff}} = 17.5$ ms [3], we set $\Delta T_2' = 15.4$ ms to produce a typical percent signal change of 2%. The baseline T_2' is set to 108.7 ms based on a typical brain T_2^* of 50 ms at $T_2 = 92.6$ ms. The fMRI time course is also affected by scanner drift and respiration induced f_0 changes. We simulated f_0 with a linearly increasing scanner drift of about 1 Hz per minute and a sinusoidal waveform (magnitude of 0.5 Hz and period of 4.2 s) to model the respiratory changes. We also added complex Gaussian random noise for a typical temporal SNR (tSNR) value of 38 dB.

B. Dictionary Selection

We solve (4) using a signal dictionary, where each dictionary atom is a point on the OSSI manifold. Because T_2, T_2', and f_0 affect OSSI signals in different ways while T_1 has a scaling effect, we constructed a 4D dictionary by varying T_2, T_2', f_0, for $T_1 = 1400$ ms. The T_2 grids were in the 40 to 150 ms range with a 1 ms spacing [36]. The T_2' grids were calculated by uniformly sampling R_2^* from 12 to 38 Hz [37] with a step size of 0.1 Hz and a fixed T_2 of 92.6 ms. We set central off-resonance frequency f_0 to [-33.3,33.3] Hz with a 0.22 Hz spacing, because OSSI signals are periodic with off-resonance frequency period = 1/TR = 66.7 Hz [3]. The 4D dictionary with axes $[T_2,\ T_2',\ f_0,\ n_c]$ has size $111 \times 261 \times 200 \times 10$. Generating the dictionary (a 1-time step) took about 7 days using Matlab with an Intel Xeon workstation with 40 CPU cores.

We reconstructed the functional signal and physics parameters from the simulated noisy fMRI time courses using the near-manifold regularizer in (3) and the 4D dictionary. The reconstructions were performed by (a) simultaneously estimating T_2 and T_2' using the 4D dictionary, (b) assuming T_2' is fixed and estimating T_2 using the 3D subset of the 4D dictionary based on the assumed T_2' value, (c) estimating T_2' with the actual T_2 value and the corresponding 3D dictionary, (d) assuming T_2 is fixed and estimating T_2' with a biased T_2 value and the corresponding 3D dictionary.

As shown in Fig. 3, because of the strong coupling between T_2 and T_2' values, it is infeasible to simultaneously estimate T_2 and T_2' (see Fig. 3a). Changes in T_2 or T_2' parameters are indistinguishable because OSSI signal shape is likely determined by the amount of signal that persists at the subsequent RF pulses, and T_2 and T_2' contribute a similar exponential decay to the persisting signals. Using a biased T_2' value for

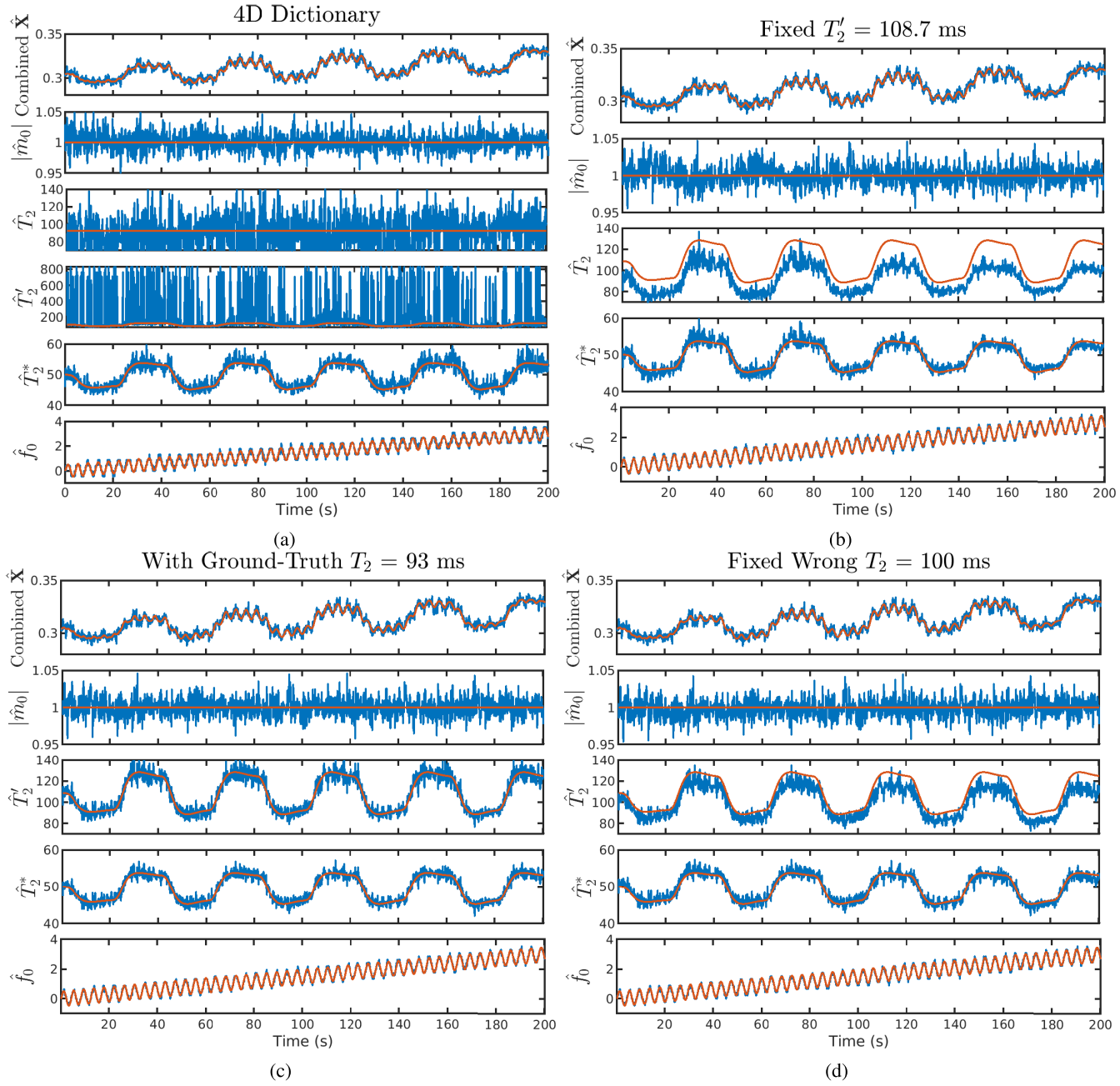

Fig. 3. Quantification results for a simulated OSSI fMRI voxel using the manifold model with 4 different choices of the manifold. The unis for $\hat{T}_2$, $\hat{T}_2'$ and $\hat{T}_2^*$ are all ms, and the units for $\hat{f}_0$ are Hz. The estimates are in blue and ground truth values are in red. Because T_2 and T_2' effects on OSSI signals are correlated (a), and a T_2 manifold does not adequately capture BOLD-induced T_2' changes (b), we use a T_2' driven physics manifold for quantification. We can estimate T_2^* and T_2' using known T_2 values (c), or use a biased guess of T_2 to quantify T_2^* (d).

T_2 estimation (Fig. 3b) or a biased T_2 value for dynamic T_2' estimation (Fig. 3d) results in noticeable bias, whereas Fig. 3c presents accurate $\hat{T}_2'$ when the ground truth T_2 is provided. However, all the different estimation approaches lead to relatively good T_2^* estimates. The coefficient of variation of $|m_0|$ estimates in Figs. 3c and 3d is 0.013, and is 0.015 and 0.014 in Figs. 3a and 3b, respectively.

Because m_0 and T_2^* estimates are more accurate in Figs. 3c and 3d, we propose to use assumed T_2 values or to measure accurate baseline T_2 maps to use for dynamic T_2^* quantification. The latter approach also provides T_2' estimates. We extended the simulation and estimation in Fig. 3d with wider ranges of fixed wrong T_2 values, and found that the T_2^* estimation remains accurate over a broad range of biased T_2 values. For example, for a ground truth T_2 of 92.6 ms, the RMSE of estimated T_2^* is less than 2 ms with a biased T_2 ranging from 67 ms to 120 ms (approximately 1 ms of the 2 ms RMSE is dictated by the noise floor of the noisy fMRI signal). Moreover, this observation remains valid for different ground truth T_2 values.

Notably, the quality of the combined functional signals is insensitive to the choice of manifold for reconstruction.

IV. Experiments

We collected ACR [38] resolution phantom data and human fMRI data to evaluate the potential of the manifold model for joint reconstruction and quantification. All the data were acquired with a 3T GE MR750 scanner (GE Healthcare, Waukesha, WI) and a 32-channel head coil (Nova Medical, Wilmington, MA).

A. Data Acquisition

OSSI acquisition parameters were the same as in Simulation Investigations with 10 s discarded data points to ensure the steady state. We selected a 2D oblique slice passing through the visual cortex with FOV $= 220 \times 220 \times 2.5\,\text{mm}^3$, matrix size $= 168 \times 168 \times 1$, and spatial resolution $= 1.3 \times 1.3 \times 2.5\,\text{mm}^3$. For OSSI, we acquired both "mostly sampled" data (for retrospective undersampling) and prospectively undersampled data. The sampling trajectories were undersampled veriable density (VD) spirals as in Fig. 1 with golden-angle based rotations between fast and slow time frames. We create VD spirals by following the principles outlined in [39] and [40]. We uniformly sample the k-space center, and linearly reduce the sampling density as the spirals extend towards the outer part of k-space. More details for implementation can be found in [6]. The "mostly sampled" data used number of interleaves $n_i = 9$ VD spirals with approximately a 1.5 undersampling factor, and temporal resolution $= 1.35$ s $=$ TR $\cdot\, n_c \cdot n_i$. The retrospective undersampling used the first interleave out of 9 for each time frame of the "mostly sampled" data. The prospective undersampling used $n_i = 1$ with temporal resolution $= 150$ ms $=$ TR $\cdot\, n_c$ Both retrospective and prospective undersampling provided $12\times$ acceleration.

For quantification evaluation, we acquired multi-echo GRE images to get standard estimates of f_0 and R_2^* values. GRE images were collected with a spin-warp sequence with TR $=$ 100 ms, Ernst flip angle $= 16°$, and different TEs $= 5.9$, 13, 26, and 40 ms. R_2^* maps were estimated based on the exponential decay of T_2^*. The field map f_0 was estimated using fully sampled GRE images at TE $= 30$ and 32 ms [41]. For the phantom data, we additionally acquired spin-echo images with a spin-warp sequence at TR $= 400$ ms and different TEs $=$ 20, 40, 60, and 80 ms to get $\hat{T}_2$ maps.

For coil sensitivity map calculation, we collected spin-warp images and used ESPIRiT [42], [43] after compressing the 32-channel coil images to 16 virtual coils using PCA [44]. The coil images were 2-norm combined for brain region extraction using the Brain Extraction Tool [45].

For human data, the functional task was a left vs. right reversing-checkerboard visual stimulus with 10 s rest followed by 5 cycles of left or right stimulus (20 s L/20 s R $\times$ 5 cycles). The 10 s resting-state data ensured the oscillating steady state and were discarded. The number of time frames (both fast time n_c and slow time) was 1490 for "mostly sampled" data and was 13340 for prospectively undersampled data.

B. Performance Evaluation

Every non-overlapping set of $n_c = 10$ fast time images were reconstructed and 2-norm combined for fMRI analysis. To avoid modeling error from the HRF of the initial rest period, the data for the first 40 s task block were discarded. The data were detrended using the first 4 discrete cosine transform basis functions to reduce effects of scanner drift.

We evaluated the functional performance of OSSIMM and comparison approaches using activation maps and tSNR maps. The backgrounds of activation maps were the mean of time-series of images. The activated regions of activation maps were determined by correlation coefficients above a 0.45 threshold. The correlation coefficients were generated by correlating the reference waveform (task and HRF related) with the fMRI time course for each voxel. For each voxel, dividing the mean of the time course by the standard deviation of the time course residual (mean and task removed) provided the tSNR map. We further calculated numbers of activated voxels at the bottom third of the brain (where the visual cortex is located) and the average tSNR values within the brain (after skull stripping).

For quantification, parameter estimations at regions with little or no signal are masked out. Specifically, we generated a mask with the first-echo GRE image (TE $= 5.9$ ms and after skull stripping) for signals larger than 10% of the signal magnitude and GRE $\hat{R}_2^* < 50$ Hz. Regions with GRE $\hat{R}_2^* > 50$ Hz are concentrated at the edge of the brain and are considered outliers. The quantitative accuracy of OSSI $\hat{R}_2^*$ was evaluated by RMSE with multi-echo GRE $\hat{R}_2^*$ as the standard. Because OSSI $\hat{f}_0$ estimates are in the range of $[-33.3, 33.3]$ Hz, we mapped the GRE $\hat{f}_0$ to the same range for comparison.

V. Reconstruction, Quantification, and Results

The proposed OSSIMM method jointly reconstructed high-resolution images and quantitative maps using the near-manifold regularizer. For both phantom and human experiments, we used the physics manifold with a fixed $T_2 =$ 100 ms unless otherwise specified. After reconstructing fast time images with mostly sampled data (OSSI-Mostly), or other models such as low-rank (OSSI-LR) and regularized cgSENSE with a spatial edge-preserving regularizer (OSSI-cgSENSE), we further estimated their parameter maps via dictionary fitting using the same manifold as in OSSIMM.

A. Implementation Details

We selected the regularization parameters based on the spectral norm $\sigma(\mathcal{A}'\mathcal{A})$, calculated with a power iteration. We set the regularization parameter β in (3) to be a fraction of $\sigma(\mathcal{A}'\mathcal{A})$ such that the condition number $\left(\sigma(\mathcal{A}'\mathcal{A}) + \beta\right)/\beta$ of the cost function was about 10 to 20 and the performance of functional maps is maximized. For example, we selected the fraction to be around 0.05 to 0.1 for all the datasets. We selected α in (6) such that the matrix rank of $\hat{\boldsymbol{X}}$ was ≈ 4 ($\alpha \approx 2\,\sigma(\mathcal{A}'\mathcal{A})$) for most fast-time image sets and to maximize the functional performance.

In OSSIMM, we used 4 iterations of alternating minimization, and 2 iterations of conjugate gradient for the data fidelity update. We used 15 iterations of POGM for the LR reconstruction and 19 iterations of conjugate gradient for

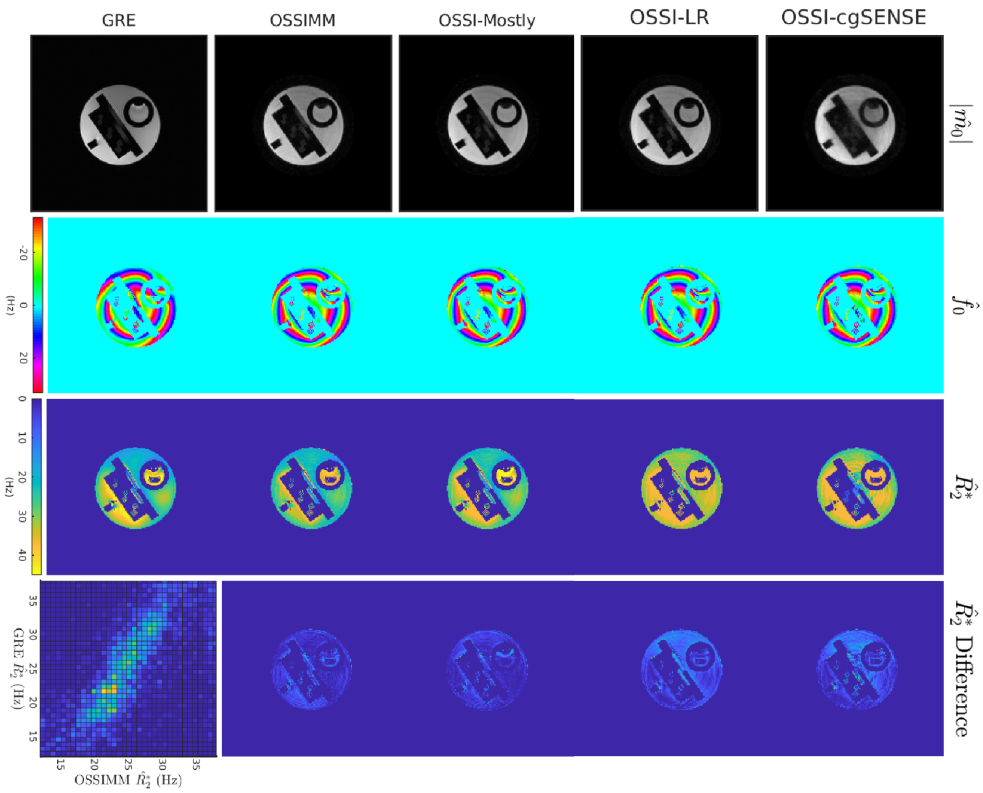

Fig. 4. Phantom quantification of m_0, f_0, and R_2^* from mostly sampled and retrospectively undersampled reconstruction using different models with comparison to multi-echo GRE. The quantification for OSSI-LR and OSSI-cgSENSE uses the proposed manifold. The $\hat{m}_0$ estimates are on arbitrary scales. The GRE $\hat{R}_2^*$ map is used as the standard for difference map calculation. The $\hat{R}_2^*$ maps and $\hat{R}_2^*$ difference maps use the same color scale. The 2D histogram (bottom left) compares OSSIMM and GRE $\hat{R}_2^*$ within the 12-38 Hz range. OSSI $\hat{R}_2^*$ and GRE $\hat{R}_2^*$ demonstrates similar contrasts.

TABLE I
PHANTOM QUANTIFICATION COMPARISON OF OSSI $\hat{R}_2^*$ TO GRE WITH OR WITHOUT A KNOWN $\hat{T}_2$ MAP

	Fixed T_2 = 100 ms		Known $\hat{T}_2$ map	
	$\hat{R}_2^*$ RMSE (Hz)	Additional Mask	$\hat{R}_2^*$ RMSE (Hz)	Additional Mask
OSSI-Mostly	4.9	4.3	5.0	4.6
OSSIMM	5.5	4.6	5.3	4.5
OSSI-LR	8.5	8.3	9	9
OSSI-cgSENSE	8.4	8.2	8.8	8.9

cgSENSE reconstruction of undersampled and mostly sampled data. We generated data-shared images as initialization for the undersampled reconstructions by using the sampling incoherence between fast and slow time [6] and combining k-space data of every 10 slow time points. We found empirically that this natural initialization worked better than the zero-filled reconstruction and performed well for the non-convex optimization of the manifold model.

B. Results

For the phantom study, Fig. 4 presents OSSI quantification results with a fixed T_2 of 100 ms. OSSIMM quantifies parameters from retrospectively undersampled data, outperforms other reconstruction methods with less residual in the different map, and yields similar maps as mostly sampled reconstruction and multi-echo GRE. The 2D histogram demonstrates a close to a linear relationship between OSSI and GRE $\hat{R}_2^*$ values. As summarized in Table I, OSSIMM led to smaller RMSE than other methods, and OSSIMM with a known $\hat{T}_2$ map produced similar results as OSSIMM with a fixed T_2 value. As demonstrated by RMSE values with additional masking in Table I, OSSIMM and OSSI-Mostly $\hat{R}_2^*$ RMSE improved by 0.5-1 Hz when a GRE $12 < \hat{R}_2^* < 38$ mask (within OSSIMM R_2^* dictionary range) is applied.

Figure 5 compares retrospectively undersampled reconstructions to the mostly sampled reference. OSSIMM reconstruction preserved high-resolution structures in oscillatory fast time images and combined images, and led to lower residuals in the difference map than LR and cgSENSE approaches.

Figure 6 presents prospectively undersampled reconstructions (temporal resolution = 150 ms) using OSSIMM, LR, and cgSENSE. OSSIMM had an activation map with more activated voxels, a time course with higher SNR, and a sharper tSNR map than other methods. The background images of the activation maps are the mean of fMRI time series using different reconstruction models. OSSIMM provided higher quality background than other methods and cgSENSE performed the worst. The functional maps from the mostly sampled reconstruction (from a different scan with a different temporal resolution = 1.35 s) are included in the last panel of Fig. 6 for reference.

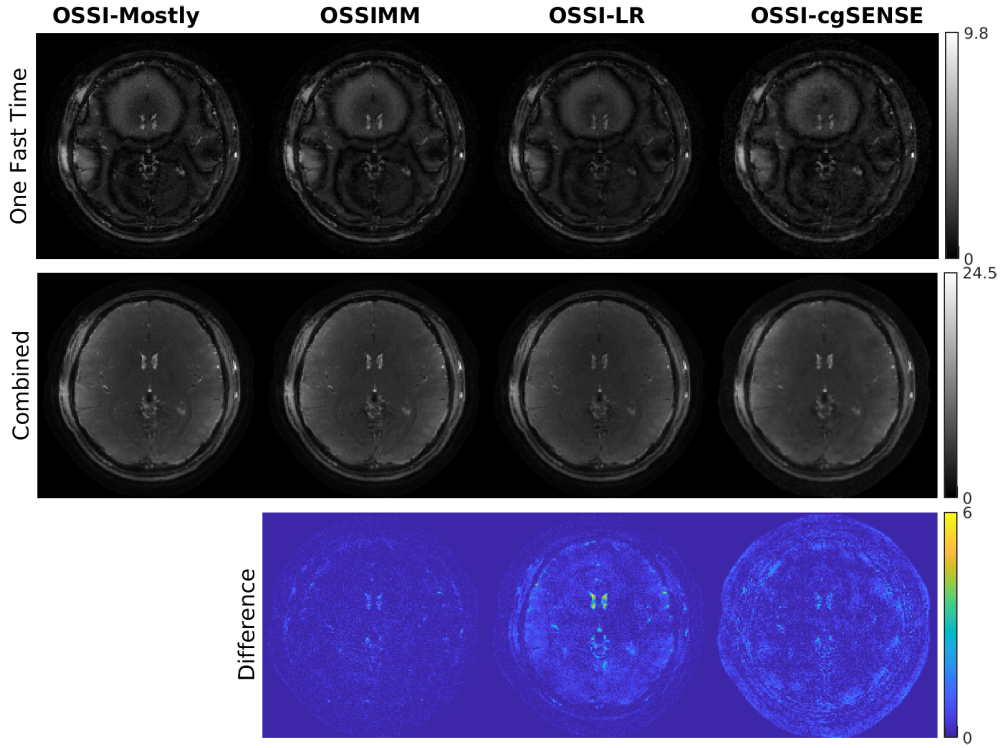

Fig. 5. Manifold, low-rank, and cgSENSE reconstructions for retrospectively undersampled OSSI data are compared to the mostly sampled reconstruction. The example fast time images present spatial variation in OSSI. OSSIMM outperforms other approaches with cleaner high-resolution details and less structure in the difference map.

Figure 7 gives retrospectively undersampled and mostly sampled OSSI quantification results with comparison to multi-echo GRE. OSSIMM with 12× undersampling leads to $\hat{m}_0$, $\hat{f}_0$, and $\hat{R}_2^*$ estimates that are almost identical to the mostly sampled case and have finer structures than OSSI-LR. OSSIMM also provides comparable $\hat{R}_2^*$ maps to GRE and demonstrates a similar distribution of $\hat{R}_2^*$ values within the brain as GRE according to the 2D histogram. Because of field drift and respiratory changes between different scans, the OSSI-Mostly and OSSIMM $\hat{f}_0$ maps are close to GRE $\hat{f}_0$ but not exactly the same.

Figure 8 compares prospectively undersampled quantification results to multi-echo GRE. OSSIMM enables high-resolution quantification of m_0, R_2^* and f_0 with a 150 ms acquisition, and yields parameter estimates more similar to GRE than LR and cgSENSE reconstructions.

The parameter maps in Figs. 7 and 8 are from a single set of $n_c = 10$ fast time images, while OSSIMM jointly reconstructs undersampled measurements and quantifies physics parameters for every 10 fast time images of the OSSI fMRI time course.

To demonstrate the dynamic quantification capacity of OSSIMM, Fig. 9 shows activation maps of $\hat{m}_0 \exp(-\hat{R}_2^* \mathrm{TE}_{\mathrm{eff}})$ and $\hat{R}_2^*$, and time courses of $\hat{R}_2^*$ at the activated regions from prospectively undersampled reconstruction (OSSIMM and cgSENSE) and quantification. OSSI $\mathrm{TE}_{\mathrm{eff}} \approx 17.5$ ms with a 2.6 ms actual TE [3].

For OSSIMM, the activation map of $\hat{m}_0 \exp(-\hat{R}_2^* \mathrm{TE}_{\mathrm{eff}})$ images well preserves R_2^* contrast of OSSI and has the same activated regions as the activation map from 2-norm combined OSSI images (in Fig. 6). The activation map from $\hat{R}_2^*$ maps recovers the activation and reduces false positives (negative activation in the positive activation region and vice versa). The colors of the activation are the opposite of activation in Fig. 6 due to the negative correlation between $m_0 \exp(-R_2^* \mathrm{TE}_{\mathrm{eff}})$ and R_2^*. The mean $\hat{R}_2^*$ map ($\overline{\hat{R}_2^*}$) of the time series, when compared to GRE, leads to a smaller RMSE value of 4.4 Hz. The RMSE value = 3.7 Hz with a GRE $12 < \hat{R}_2^* < 38$ Hz mask.

OSSIMM also provided higher quality dynamic quantification results than cgSENSE, with more functional activation in the activation maps computed from $\hat{m}_0 \exp(-\hat{R}_2^* \mathrm{TE}_{\mathrm{eff}})$ and $\hat{R}_2^*$, and less noisy time courses of $\hat{R}_2^*$ in the activated regions (same region of interest as the time courses in Fig. 6).

TABLE II
HUMAN RECONSTRUCTION AND R_2^* QUANTIFICATION EVALUATION FOR DIFFERENT SAMPLING PATTERNS AND MODELS

	OSSIMM	OSSI-LR	OSSI-cgSENSE	OSSI-Mostly
Retrospectively Undersampled				
$\hat{R}_2^*$ RMSE (Hz)	5.1	6.6	5.4	5.1
Additional Mask	4.5	6.1	4.9	4.5
Prospectively Undersampled				
$\hat{R}_2^*$ RMSE (Hz)	4.9	6.7	5.5	-
Additional Mask	4.3	6.4	5.0	-
# Activated Voxels	181	159	68	-
Average tSNR	26.4	26.5	18.8	-

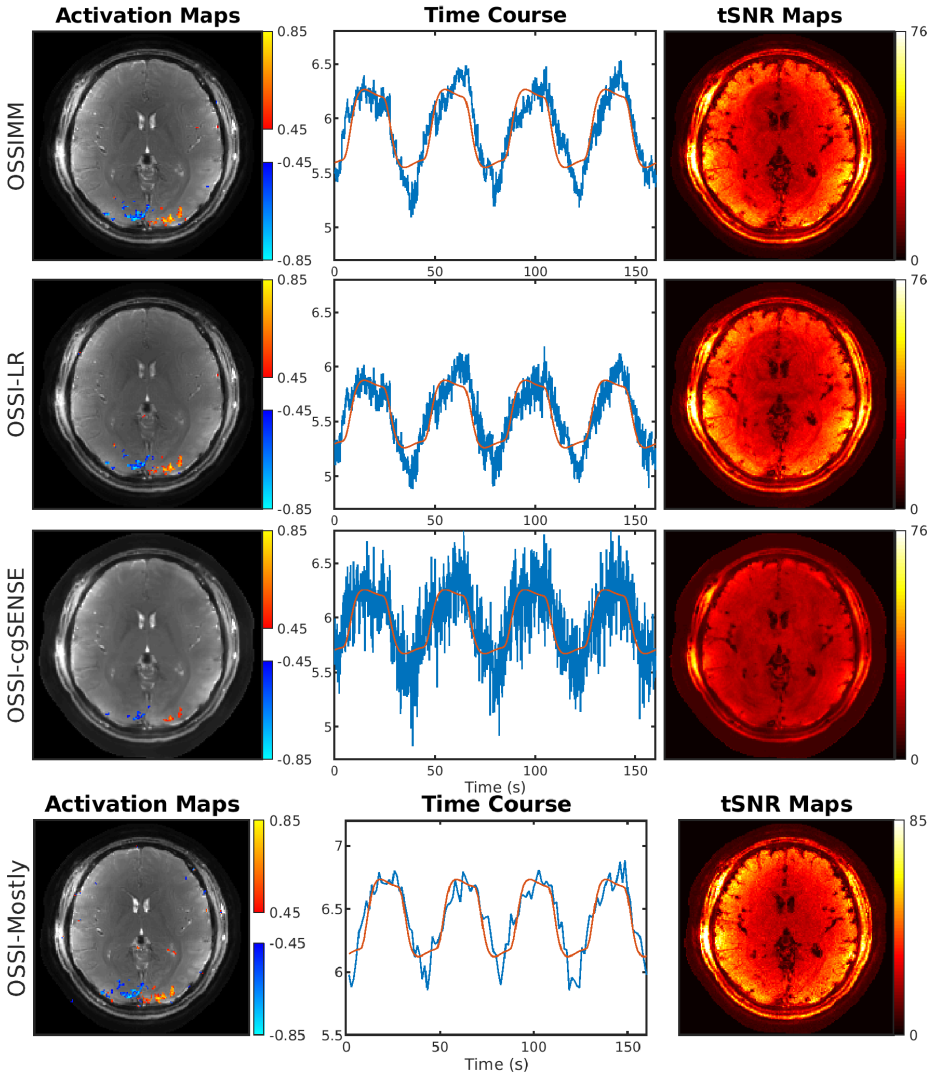

Fig. 6. Functional results for prospectively undersampled data (first 3 rows) with temporal resolution of 150 ms and spatial resolution of 1.3 mm. The proposed OSSIMM reconstruction provides an activation map with high-resolution background image and larger activated regions, and time course (reference waveform in red) and temporal SNR map with higher SNR than other methods. As a reference only to demonstrate the expected regions of activation in the brain for the visual task, the last row provides mostly sampled functional maps from a different scan of the same subject with a different temporal resolution of 1.35 s and spatial resolution of 1.3 mm.

Table II summarizes quantitative evaluations of different sampling schemes and reconstruction models. OSSI $\hat{R}_2^*$ RMSE values compared to GRE for retrospectively (Fig. 7) and prospectively (Fig. 8) undersampling are presented. As demonstrated by RMSE values with additional masking, OSSI RMSE decrease by about 0.5 Hz with the GRE $12 < \hat{R}_2^* < 38$ mask. The last two rows of the table correspond to Fig. 6 and are numbers of activated voxels and average tSNR within the brain for prospectively undersampled reconstructions. The proposed OSSIMM jointly reconstructs high-resolution images with more functional activation and parameter maps with smaller $\hat{R}_2^*$ RMSE than other approaches.

VI. Discussion

We propose a novel manifold model OSSIMM that uses MR physics for the signal generation as the regularizer for image reconstruction from undersampled k-space data. The proposed model simultaneously provides high-resolution fMRI images and quantitative maps of important MRI physics parameters.

The proposed near-manifold regularizer has the advantage of allowing for potential imperfections of the manifold model. Instead of requiring the signal values to lie exactly on the manifold, it provides a balance between fitting the fast-time images to the noisy k-space data and to the manifold. For reconstruction, OSSIMM outperforms low-rank and cgSENSE models by providing more functional activation, without spatial or temporal smoothing.

For quantification, OSSIMM dynamically tracks m_0, R_2^*, and f_0 changes with a temporal resolution of 150 ms in our experiments. The OSSIMM estimates $\hat{m}_0 \exp(-\hat{R}_2^* \mathrm{TE}_{\mathrm{eff}})$ or $\hat{R}_2^*$ contain most of the functional information of fMRI time series, and may be well-suited for examining quantitative changes in longitudinal studies. Moreover, OSSIMM quantifies parameters with acquisition time of 150 ms per slice, which is faster than other quantification methods such as [22]. The

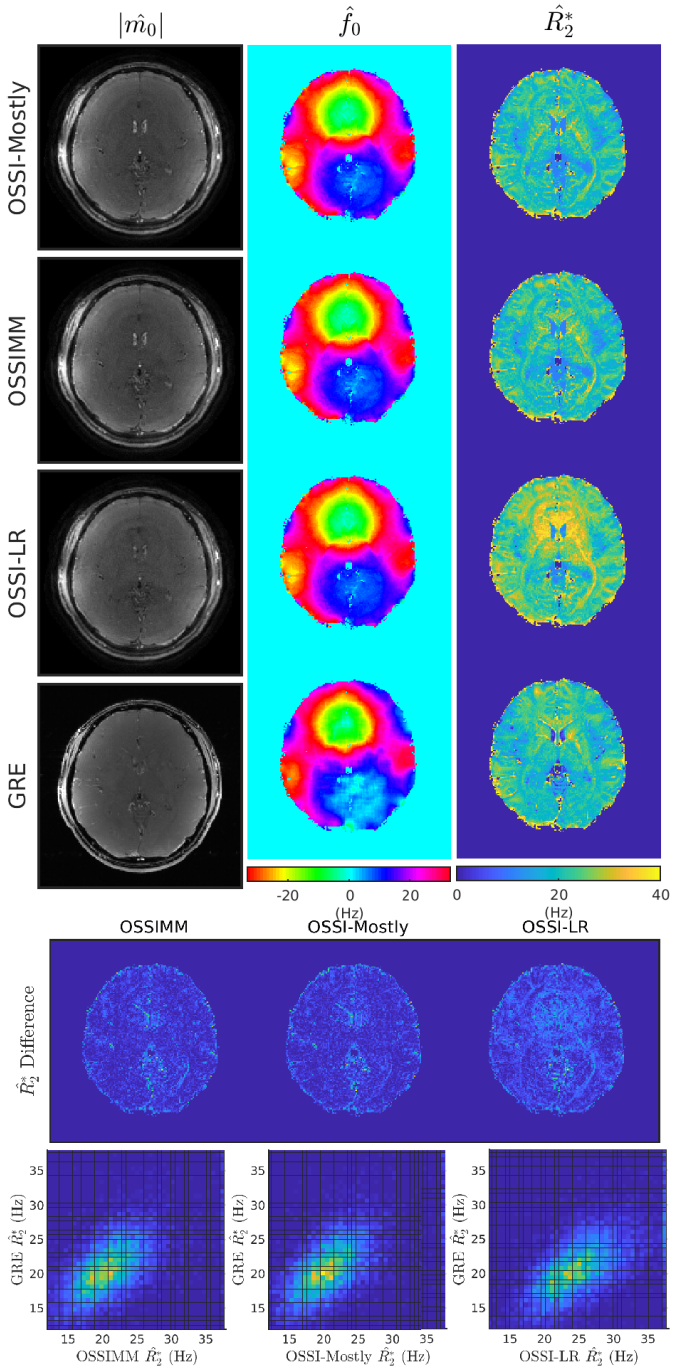

Fig. 7. Retrospectively undersampled quantifications and comparison to multi-echo GRE estimates. OSSIMM presents similar results as the mostly sampled data. $\hat{R}_2^*$ difference maps (using GRE $\hat{R}_2^*$ as standard and of same color scale as $\hat{R}_2^*$ maps) and 2D histogram of $\hat{R}_2^*$ values show that OSSIMM provides comparable quantitative maps to GRE.

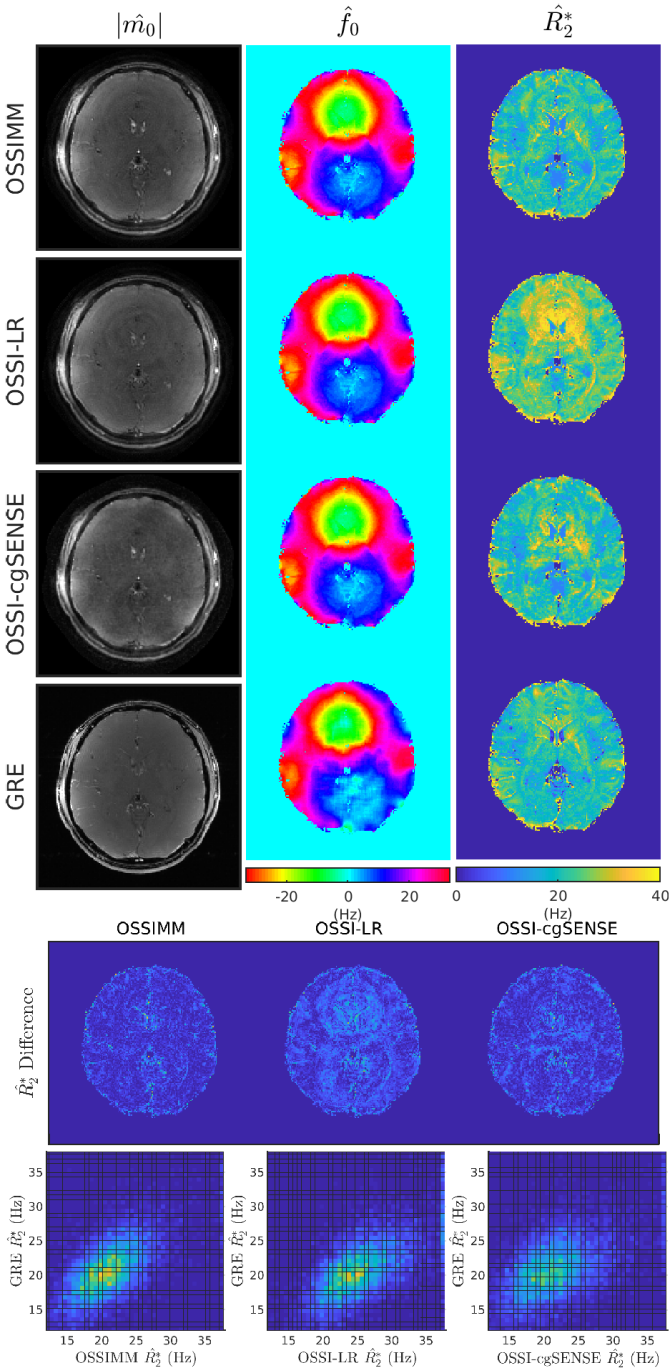

Fig. 8. Prospectively undersampled quantifications compared to multi-echo GRE. OSSIMM results in reasonable parameter maps with 1.3 mm spatial resolution and a 150 ms acquisition time. OSSIMM also outperforms low-rank and cgSENSE reconstructions with less residual in the $\hat{R}_2^*$ difference map (same color scale as $\hat{R}_2^*$ maps).

manifold model and the near-manifold regularization can be generalized to other sparsely undersampled datasets for joint reconstruction and quantification.

The LR model enforces low-rankness on every set of n_c fast time images, causing spatial-temporal smoothing along fast time. Therefore, the LR reconstructed fast time signal values are less accurate for parameter quantification (dictionary fitting with voxel-wise fast time signal values), and the parameter estimates from LR reconstruction deviate more from the ground truth values than other models. The average tSNR value from LR reconstruction was 0.1 higher than OSSIMM, potentially (Table II) due to the spatial-temporal smoothing effects of the LR model.

There are multiple factors that contribute to slight mismatches between OSSI $\hat{R}_2^*$ and GRE $\hat{R}_2^*$. The OSSI and GRE images were not exactly aligned due to different gradient delays or the movement of the brain between different scans, especially around the edge of the brain. It is also possible

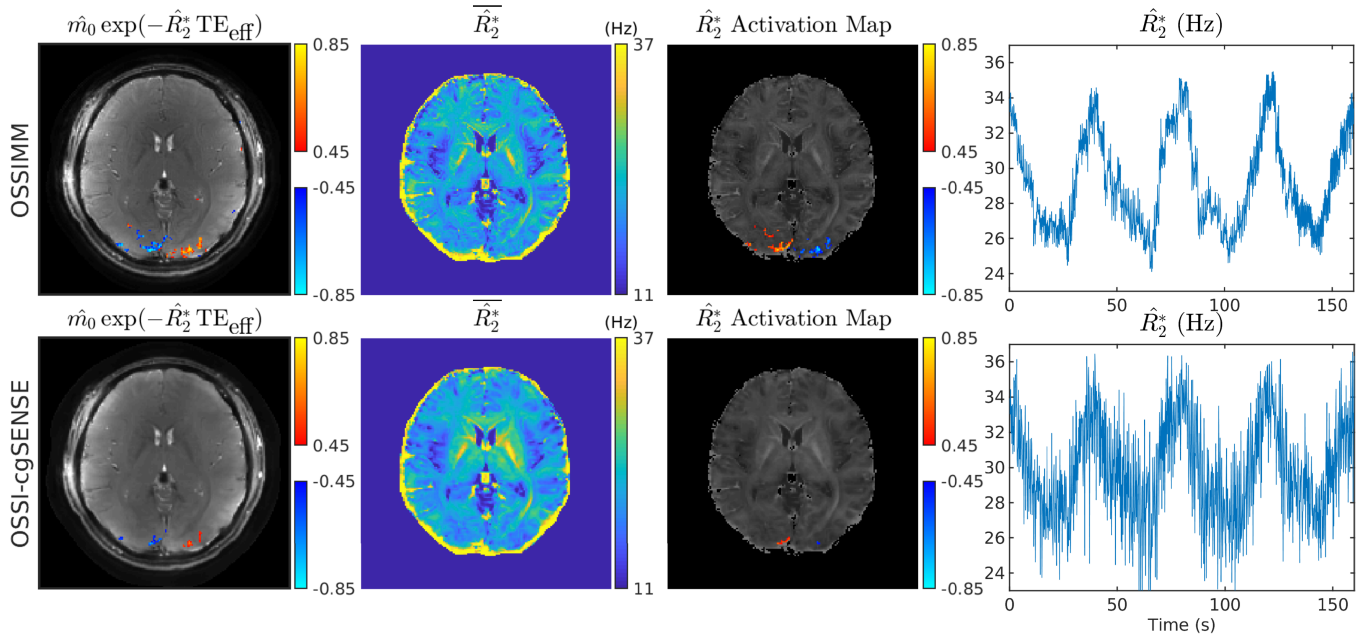

Fig. 9. OSSIMM (top row) and OSSI-cgSENSE (bottom row) activation maps computed from $\hat{m}_0$ and $\hat{R}_2^*$ with prospective undersampling, demonstrating the dynamic quantification capacity of OSSIMM. Both time series of $\hat{m}_0 \exp(-\hat{R}_2^* \mathrm{TE}_{\mathrm{eff}})$ (left) and $\hat{R}_2^*$ (right) almost fully recover the functional activation. The $\overline{\hat{R}_2^*}$ (middle) is the mean of $\hat{R}_2^*$ time series after skull stripping (without any other mask) and well preserves the R_2^* contrast.

that through-plane gradients change signals slightly differently between OSSI and GRE. The OSSIMM implementation could be improved with a larger dictionary with a larger range of R_2^* values and finer spacing of the varying physics parameters.

The proposed near-manifold regularizer can accommodate mismatches due to model simplification and nonidealities in experiments. We neglected the readout length effect for simplicity and have not performed field map correction for human data. The intravoxel dephasing during the readout is small because the readout length is less than 10 ms. More accurate models might be helpful for acquisitions with longer readouts. We simulated and found that the flip angle variation of about $+/-20\%$ of the excitation flip angle affects the OSSI signal mostly as a scaling factor. Therefore, RF inhomogeneity and imperfections in excitation profiles can be addressed by the scaling parameter m_0 and the near manifold regularization. The field map correction improves quantification for phantom data, but would increase computation for human fMRI time series. One interesting extension would be to dynamically quantify f_0 and correct for field inhomogeneity using the time-series of OSSI $\hat{f}_0$ maps. Because OSSI $\hat{f}_0$ maps are in the range of $[-33.3, 33.3]$ Hz, we could use an initial estimate of $\hat{f}_0$ from two-echo GRE, and dynamically update the initial $\hat{f}_0$ based on OSSI $\hat{f}_0$ changes along time as in [25]. Other nonidealities include non-Lorentzian frequency distribution, e.g., through-plane inhomogeneity may be closer to a linear distribution of frequencies, and in-flow effects.

We believe that the reconstruction performance can be further improved with spatial-temporal modeling of OSSI fMRI image series. We will combine OSSIMM with the patch-tensor low-rank model [6] to exploit different aspects of prior information (linear and nonlinear) and enable more aggressive undersampling. We will apply the 3D OSSI acquisition in [6], and extend the OSSIMM dynamic quantification to 3D fMRI joint reconstruction and quantification.

OSSI can provide similar T_2^*-weighting and off-resonance sensitivity with different combinations of TR, n_c, and flip angle [3]. Therefore, for different temporal resolutions with short TRs and appropriate n_c values, we expect the manifold model to work well, and the main change would be to construct new dictionaries with a new set of scanning parameters.

VII. Conclusion

This paper proposes OSSIMM, a novel reconstruction and quantification model for nonlinear MR signals. With a factor of 12 undersampling and without spatial or temporal smoothing, OSSIMM outperforms other reconstruction models with high-resolution structures and more functional activation. OSSIMM also provides dynamic R_2^* maps that are comparable to GRE $\hat{R}_2^*$ maps with a 150 ms temporal resolution.

Acknowledgment

The authors would like to thank Dr. Amos Cao for important discussions on signal modeling and Dinank Gupta for helping with spin-echo imaging.

References

[1] S. Ogawa, T.-M. Lee, A. S. Nayak, and P. Glynn, "Oxygenation-sensitive contrast in magnetic resonance image of rodent brain at high magnetic fields," *Magn. Reson. Med.*, vol. 14, no. 1, pp. 68–78, Apr. 1990.

[2] D. C. Noll, "A primer on MRI and functional MRI," Dept. Biomed. Eng., Univ. Michigan, Arbor, Michigan, Tech. Rep., 2001.

[3] S. Guo and D. C. Noll, "Oscillating steady-state imaging (OSSI): A novel method for functional MRI," *Magn. Reson. Med.*, vol. 84, no. 2, pp. 698–712, Aug. 2020.

[4] O. Bieri and K. Scheffler, "Fundamentals of balanced steady state free precession MRI," *J. Magn. Reson. Imag.*, vol. 38, no. 1, pp. 2–11, Jul. 2013.

[5] Y. Zur, M. L. Wood, and L. J. Neuringer, "Spoiling of transverse magnetization in steady-state sequences," *Magn. Reson. Med.*, vol. 21, no. 2, pp. 251–263, Oct. 1991.

[6] S. Guo, J. A. Fessler, and D. C. Noll, "High-resolution oscillating steady-state fMRI using patch-tensor low-rank reconstruction," *IEEE Trans. Med. Imag.*, vol. 39, no. 12, pp. 4357–4368, Dec. 2020.

[7] S. Guo, D. C. Noll, and J. A. Fessler, "Dictionary-based oscillating steady state fMRI reconstruction," in *Proc. 27th Annu. Meeting ISMRM*, Montreal, QC, Canada, 2019, p. 1253.

[8] V. Roeloffs, S. Rosenzweig, H. C. M. Holme, M. Uecker, and J. Frahm, "Frequency-modulated SSFP with radial sampling and subspace reconstruction: A time-efficient alternative to phase-cycled bSSFP," *Magn. Reson. Med.*, vol. 81, no. 3, pp. 1566–1579, Mar. 2019.

[9] B. Zhao, K. Setsompop, H. Ye, S. F. Cauley, and L. L. Wald, "Maximum likelihood reconstruction for magnetic resonance fingerprinting," *IEEE Trans. Med. Imag.*, vol. 35, no. 8, pp. 1812–1823, Aug. 2016.

[10] J. Assländer, M. A. Cloos, F. Knoll, D. K. Sodickson, J. Hennig, and R. Lattanzi, "Low rank alternating direction method of multipliers reconstruction for MR fingerprinting," *Magn. Reson. Med.*, vol. 79, no. 1, pp. 83–96, Jan. 2018.

[11] Y. Bengio, A. Courville, and P. Vincent, "Representation learning: A review and new perspectives," *IEEE Trans. Pattern Anal. Mach. Intell.*, vol. 35, no. 8, pp. 1798–1828, Aug. 2013.

[12] Z. Ke et al., "Deep manifold learning for dynamic MR imaging," *IEEE Trans. Comput. Imag.*, vol. 7, pp. 1314–1327, Dec. 2021.

[13] S. Abdullah, O. Arif, M. Bilal Arif, and T. Mahmood, "MRI reconstruction from sparse K-space data using low dimensional manifold model," *IEEE Access*, vol. 7, pp. 88072–88081, 2019.

[14] S. Arberet et al., "A parallel spatial and bloch manifold regularized iterative reconstruction method for MR fingerprinting," *Magn. Reson. Imag.*, vol. 82, pp. 74–90, Oct. 2021.

[15] J. Gonzalez-Castillo, I. S. Fernandez, K. C. Lam, D. A. Handwerker, F. Pereira, and P. A. Bandettini, "Manifold learning for fMRI time-varying functional connectivity," *Frontiers Human Neurosci.*, vol. 17, Jul. 2023.

[16] S. Gao, G. Mishne, and D. Scheinost, "Nonlinear manifold learning in functional magnetic resonance imaging uncovers a low-dimensional space of brain dynamics," *Human Brain Mapping*, vol. 42, no. 14, pp. 4510–4524, Oct. 2021.

[17] K. Kumar, M. Toews, L. Chauvin, O. Colliot, and C. Desrosiers, "Multi-modal brain fingerprinting: A manifold approximation based framework," *Neuroimage*, vol. 183, pp. 212–226, Dec. 2018.

[18] G. Dong, M. Hintermüller, and K. Papafitsoros, "Quantitative magnetic resonance imaging: From fingerprinting to integrated physics-based models," *SIAM J. Imag. Sci.*, vol. 12, no. 2, pp. 927–971, Jan. 2019.

[19] J. I. Tamir, F. Ong, S. Anand, E. Karasan, K. Wang, and M. Lustig, "Computational MRI with physics-based constraints: Application to multicontrast and quantitative imaging," *IEEE Signal Process. Mag.*, vol. 37, no. 1, pp. 94–104, Jan. 2020.

[20] X. He and D. A. Yablonskiy, "Quantitative BOLD: Mapping of human cerebral deoxygenated blood volume and oxygen extraction fraction: Default state," *Magn. Reson. Med.*, vol. 57, no. 1, pp. 115–126, Jan. 2007.

[21] W. D. Penny, K. J. Friston, J. T. Ashburner, S. J. Kiebel, and T. E. Nichols, *Statistical Parametric Mapping: The Analysis of Functional Brain Images*. Amsterdam, The Netherlands: Elsevier, 2011.

[22] C. Y. Wang, S. Coppo, B. B. Mehta, N. Seiberlich, X. Yu, and M. A. Griswold, "Magnetic resonance fingerprinting with quadratic RF phase for measurement of T_2^* simultaneously with δ_f, T_1, and T_2," *Magn. Reson. Med.*, vol. 81, no. 3, pp. 1849–1862, 2019.

[23] O. Speck and J. Hennig, "Functional imaging by I_0- and T_2^*-parameter mapping using multi-image EPI," *Magn. Reson. Med.*, vol. 40, no. 2, pp. 243–248, 1998.

[24] A. B. Wennerberg, T. Jonsson, H. Forssberg, and T.-Q. Li, "A comparative fMRI study: T2*-weighted imaging versus R2* mapping," *NMR Biomed.*, vol. 14, no. 1, pp. 41–47, 2001.

[25] V. T. Olafsson, D. C. Noll, and J. A. Fessler, "Fast joint reconstruction of dynamic R_2^* and field maps in functional MRI," *IEEE Trans. Med. Imag.*, vol. 27, no. 9, pp. 1177–1188, Sep. 2008.

[26] G. H. Golub and V. Pereyra, "The differentiation of pseudo-inverses and nonlinear least squares problems whose variables separate," *SIAM J. Numer. Anal.*, vol. 10, no. 2, pp. 413–432, Apr. 1973.

[27] G. Golub and V. Pereyra, "Separable nonlinear least squares: The variable projection method and its applications," *Inverse Problems*, vol. 19, no. 2, pp. R1–R26, Apr. 2003.

[28] J. Fessler. *Michigan Image Reconstruction Toolbox*. Accessed: Jan. 16, 2020. [Online]. Available: https://web.eecs.umich.edu/~fessler/code/index.html

[29] J. A. Fessler, "Optimization methods for magnetic resonance image reconstruction: Key models and optimization algorithms," *IEEE Signal Process. Mag.*, vol. 37, no. 1, pp. 33–40, Jan. 2020.

[30] D. Kim and J. A. Fessler, "Adaptive restart of the optimized gradient method for convex optimization," *J. Optim. Theory Appl.*, vol. 178, no. 1, pp. 240–263, Jul. 2018.

[31] A. B. Taylor, J. M. Hendrickx, and F. Glineur, "Exact worst-case performance of first-order methods for composite convex optimization," *SIAM J. Optim.*, vol. 27, no. 3, pp. 1283–1313, Jan. 2017.

[32] C. Y. Lin and J. A. Fessler, "Efficient dynamic parallel MRI reconstruction for the low-rank plus sparse model," *IEEE Trans. Comput. Imag.*, vol. 5, no. 1, pp. 17–26, Mar. 2019.

[33] (2020). *Relaxation Times*. Accessed: Jan. 16, 2020. [Online]. Available: https://itis.swiss/virtual-population/tissue-properties/database/relaxation-times/

[34] *Statistical Parametric Mapping*. Accessed: Jan. 16, 2020. [Online]. Available: https://www.fil.ion.ucl.ac.uk/spm/

[35] T. Jin, P. Wang, M. Tasker, F. Zhao, and S. Kim, "Source of nonlinearity in echo-time-dependent BOLD fMRI," *Magn. Reson. Med.*, vol. 55, no. 6, pp. 1281–1290, Jun. 2006.

[36] D. Ma et al., "Magnetic resonance fingerprinting," *Nature*, vol. 495, no. 7440, pp. 187–192, Mar. 2013.

[37] P. Péran et al., "Voxel-based analysis of R2* maps in the healthy human brain," *J. Magn. Reson. Imag.*, vol. 26, no. 6, pp. 1413–1420, Dec. 2007.

[38] *ACR Phantom*. Accessed: Jun. 13, 2022. [Online]. Available: https://www.acraccreditation.org/-/media/ACRAccreditation/Documents/MRI/ACR-Large–Med-Phantom-GuidanceFinal.pdf

[39] B. Hargreaves. *Variable-Density Spiral Design Functions*. Accessed: Jun. 16, 2020. [Online]. Available: http://mrsrl.stanford.edu/~brian/vdspiral/

[40] J. H. Lee, B. A. Hargreaves, B. S. Hu, and D. G. Nishimura, "Fast 3D imaging using variable-density spiral trajectories with applications to limb perfusion," *Magn. Reson. Med.*, vol. 50, no. 6, pp. 1276–1285, Dec. 2003.

[41] D. C. Noll, J. D. Cohen, C. H. Meyer, and W. Schneider, "Spiral K-space MR imaging of cortical activation," *J. Magn. Reson. Imag.*, vol. 5, no. 1, pp. 49–56, Jan. 1995.

[42] M. Uecker et al., "ESPIRiT—An eigenvalue approach to autocalibrating parallel MRI: Where SENSE meets GRAPPA," *Magn. Reson. Med.*, vol. 71, no. 3, pp. 990–1001, Mar. 2014.

[43] M. Uecker et al., "Berkeley advanced reconstruction toolbox," in *Proc. 23th Annu. Meeting ISMRM*, Montreal, QC, Canada, 2015, p. 2486.

[44] F. Huang, S. Vijayakumar, Y. Li, S. Hertel, and G. R. Duensing, "A software channel compression technique for faster reconstruction with many channels," *Magn. Reson. Imag.*, vol. 26, no. 1, pp. 133–141, Jan. 2008.

[45] S. M. Smith, "Fast robust automated brain extraction," *Hum. Brain Mapping*, vol. 17, no. 3, pp. 143–155, Nov. 2002.